Particle Accelerators, Vol. 62, pp. 215–239
Reprints available directly from the publisher
Photocopying permitted by license only

A THEORY OF LOW FREQUENCY FAR-FIELD SYNCHROTRON RADIATION

F. MÉOT *

CEA, DSM/DAPNIA/SEA, CEA-Saclay, F-91191 Gif sur Yvette, France

(Received 23 February 1998; In final form 10 July 1998)

Properties of synchrotron radiation (SR) are addressed in terms of the behaviour of the radiated wave electric field. Based on this method a simple theory of low frequency far-field SR is established – liable to reach up to X-ray energy ranges in sufficiently high energy lepton machines; spectral angular distributions and other properties are derived. As a direct outcome, it is shown that a $(2/\gamma)$-deviation dipole produces highest brightness in the low frequency spectral range with a gain of four w.r.t. edge SR and up to several orders of magnitude w.r.t. body SR from a long dipole. Numerical examples are given.

Keywords: Synchrotron radiation; Infrared SR; Edge radiation

1 INTRODUCTION

Low frequency synchrotron radiation (SR) has always been a concern in many respects, e.g., as to beam diagnostics with visible light in medium energy machines and up to X-rays in highest energy machines. It is now also becoming a hotter topic for the sake of quality long-wavelength radiation production in last generation SR rings such as the SOLEIL project,[1] as well as in existing machines.

Properties of SR can be efficiently addressed in terms of the behaviour of the radiated wave electric field. The method has long been used in the case of weak SR[2,3] and proved to be efficient in strong SR studies as well.[4–7] In this paper we establish by this means a simple theory of

* E-mail: fmeot@cea.fr.

low frequency, far-field SR and we review several related properties. The material so developed provides the right understanding where classical theory of SR cannot; it allows precise calculation of SR intensity and angular distributions.

As a direct outcome we show how low frequency SR properties cause a $(2/\gamma)$-deviation dipole to shift the SR peak energy density to the low frequency spectral range – liable to reach up to X-ray energy ranges in sufficiently high energy lepton machines, entailing a gain of four w.r.t. edge SR and up to several orders of magnitude w.r.t. body SR from a long dipole, and confinement of the radiation within $\sqrt{2}/\gamma$ rms aperture cone. Comparisons with edge and body SR are performed and numerical examples are given.

2 SR ELECTRIC FIELD

The SR spectral angular energy density is given by[8]

$$\frac{\partial^2 W}{\partial\omega\partial\Omega} = 2\epsilon_0 cr^2 |\tilde{\vec{E}}(\omega)|^2, \tag{1}$$

where r is the distance (assumed constant) from the particle trajectory region to the observer, $\tilde{\vec{E}}(\omega)$ the Fourier transform of the electric field $\vec{E}(t)$ of the radiated wave, $\omega/2\pi$ the spectral frequency and Ω the solid angle. In the far-field approximation ($r \ll r^2$) the electric field of the radiated electromagnetic wave writes (see notations in Figure 1)

$$\vec{E}(t) = \frac{q}{4\pi\epsilon_0 c} \frac{\vec{n}(t') \times [(\vec{n}(t') - \vec{\beta}(t')) \times \dot{\vec{\beta}}(t')]}{r(t')(1 - \vec{n}(t') \cdot \vec{\beta}(t'))^3} \tag{2}$$

with

$$t' = t - r(t')/c \tag{3}$$

and t = observer time, t' = particle time, $\vec{n}(t') = \vec{r}(t')/r(t')$ = observer direction, $c\vec{\beta}(t')$ = particle velocity, $\dot{\vec{\beta}}(t') = \mathrm{d}\vec{\beta}/\mathrm{d}t'$, q = charge. $\vec{E}$ is normal to $\vec{n}$ and can be split into the two polarisation components $\vec{E}_\sigma$ parallel to the bend plane and $\vec{E}_\pi$ normal to $\vec{E}_\sigma$ and $\vec{n}$.

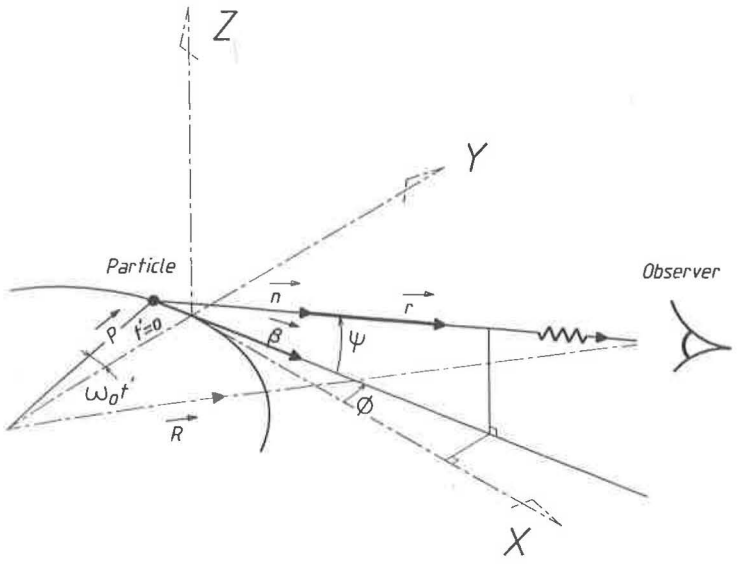

FIGURE 1 Reference laboratory frame and notations used in the text. The particle rotates with $\omega_0 = c/\rho$ velocity; its radiation is observed at large distance r (assumed constant) under arbitrary aiming (ϕ, ψ).

3 LOW FREQUENCY SR

Properties of the integral in Eq. (1) can be inferred from properties of the integrand in the Fourier transform $\tilde{\vec{E}}(\omega)$ that is, from $\vec{E}(t)$ (Eq. (2)). Furthermore in the case of low frequency SR the Fourier transform for a Δt-long impulse verifies $\tilde{\vec{E}}(\omega) \approx (1/\sqrt{2\pi}) \int_{\Delta t} \vec{E}(t) e^{-i\omega t}\, dt|_{\omega \approx 0}$, which leads to

$$\tilde{\vec{E}}(\omega) \approx \frac{1}{\sqrt{2\pi}} \int_{\Delta t} \vec{E}(t)\, dt \tag{4}$$

independent of the frequency ω under observation. This integral can be calculated in particle time variable t' under the form

$$\tilde{\vec{E}}(\omega) \approx \frac{1}{\sqrt{2\pi}} \int_{\Delta t} \vec{E}(t') \frac{dt}{dt'}\, dt' \tag{5}$$

with $E(t') \equiv E(t(t'))$ while the $t(t')$ dependence can be obtained from Eq. (3) that also provides, by differentiation expanded to order $(1/\gamma^2)$

$$dt/dt' = 1 - \vec{n}(t') \cdot \vec{\beta}(t') \simeq [1 + \gamma^2\psi^2 + \gamma^2(\omega_0 t' - \phi)^2]/2\gamma^2 \quad (6)$$

following notations explicited in Section 3.2 and Figure 1.

3.1 Frequency Validity Domain

As stated above the low frequency approximation is valid as long as $\omega\Delta t \ll 1$, where Δt is the total duration of the observed impulse and can be obtained from Eq. (11) with $t' = L/2c$, where L is the magnetic field extent. In the forward direction ($\psi = 0$) this gives

$$\Delta t = L(1 + \gamma^2\alpha^2/12)/2\gamma^2 c \quad (7)$$

where $\alpha = \omega_0 L/c = L/\rho$ is the total deviation and ρ is the curvature radius. One therefore gets the validity condition

$$\omega \ll 2\gamma^2 c/L(1 + \gamma^2\alpha^2/12). \quad (8)$$

As an example consider a 2.5 GeV electron subject to $\alpha \approx 20/\gamma$ deviation in a $L = 0.2$ m long dipole ($\rho \approx 50$ m); the model requires that (Eq. (8) with $\gamma\alpha \gg 1$) $\omega \ll 24c/\alpha^2 L \approx 2 \times 10^{15}$ rad s^{-1}, i.e., rather long wavelengths $\lambda \gg 1\,\mu$m; on the other hand, a weaker magnet with $\rho \approx 500$ m, deviation $\alpha = 2/\gamma$ (hence, length $L = 2\rho/\gamma$; such magnet provides higher low frequency intensity, see Section 4) leads to much higher frequency validity limit $\omega \ll 3\gamma^3 c/4\rho \equiv \omega_c/2 \approx 5 \times 10^{16}$ rad s^{-1} ($\lambda \gg 0.04\,\mu$m).

At 45 GeV in LEP in a $\rho = 1300$ m, $L = 0.5$ m long dipole ($\alpha \approx 35/\gamma$) validity of the model demands that $\omega \ll 24c/\alpha^2 L \approx 10^{17}$ rad s^{-1} ($\lambda \gg 0.02\,\mu$m); this condition is for instance fairly fulfilled in the *visible light* ($\lambda \approx 0.4\,\mu$m) diagnostic experiments reported in Ref. [6] which shows excellent consistency with the formalism developed hereafter.

3.2 Electric Field in Particle Time

Following regular notations we take[8] (Figure 1) $\vec{r}(t') = \vec{R} - \vec{p}(t') \approx$ constant with $\vec{R}$ (resp. $\vec{p}(t')$) = position of the observer (particle) in the

laboratory frame, and ϕ (resp. ψ) = horizontal (vertical) component of the observation angle (ϕ is zero in the direction coinciding with $\omega_0 t' = 0$), $\omega_0 = c/\rho$ = rotation frequency with ρ = constant bending radius. In the (x, y, z) frame this leads to

$$\vec{n} = (\cos\psi\cos\phi,\ \cos\psi\sin\phi,\ \sin\psi), \quad \vec{\beta} = \beta(\cos\omega_0 t',\ \sin\omega_0 t', 0). \quad (9)$$

Substituting in Eq. (2) one gets the electric field impulse from a $(2cT')$-long dipole, as split into the two components introduced in Section 2

$$E_\sigma(t') = \frac{q\omega_0\gamma^4}{\pi\epsilon_0 cr}\,\frac{(1+\gamma^2\psi^2) - \gamma^2(\omega_0 t' - \phi)^2}{(1+\gamma^2\psi^2+\gamma^2(\omega_0 t'-\phi)^2)^3}\ \mathrm{rect}(t'/2T'),$$

$$E_\pi(t') = \frac{q\omega_0\gamma^4}{\pi\epsilon_0 cr}\,\frac{-2\gamma\psi\gamma(\omega_0 t' - \phi)}{(1+\gamma^2\psi^2+\gamma^2(\omega_0 t'-\phi)^2)^3}\ \mathrm{rect}(t'/2T') \quad (10)$$

where $\mathrm{rect}(x) = 1$ if $-\frac{1}{2} < x < \frac{1}{2}$ and zero elsewhere, allowing for the finite extent of the magnetic field. By taking such "rect" field model we neglect possible effects of smooth field fall-off at magnet ends. On the one hand sharper end field mostly affects the high frequency spectrum domain;[2] on the other hand, the "rect" model is justified as long as the edge extent remains much shorter than the magnet length, as has been shown with some detail in previous publications.[5,9]

It can be observed from the equations above taken with $\phi = 0$, that the sign of $E_\sigma(t')$ goes with that of the bending radius ρ (due to the $\omega_0^3 = c^3/\rho^3$ dependence), contrary to $E_\pi(t')$ (ω_0^2 dependence). This plays an important role in the low frequency range, in possible decrease or increase of interference effects between neighbouring SR sources, as shown in Refs. [5,11].

Note that $E_\sigma(t')$ is zero at $\tau_c' = \phi/\omega_0 \pm \sqrt{1+\gamma^2\psi^2}/\gamma\omega_0$ in particle time; this corresponds to $2\omega_o\tau_c' = 2/\gamma$ deviation in the laboratory frame. The related half-width τ_c of $E_\sigma(t)$ in observer time can be obtained from Eqs. (3), (9) (or by integration of Eq. (6) as well) with $\phi = 0$ which (given that $\omega_0 t' \ll 1$) leads to

$$t = t'(1+\gamma^2\psi^2)/2\gamma^2 + c^2 t'^3/6\rho^2 \quad (11)$$

and by taking $t' = \tau_c'$, which gives $\tau_c = \pm(1+\gamma^2\psi^2)^{3/2}/\omega_c$, with $\omega_c = 3\gamma^3 c/2\rho$ = critical frequency. It can also be pointed out that $E_{\sigma,\pi}(t')$ have shapes similar to $E_{\sigma,\pi}(t)$ as seen by the observer (Figure 2(a)) whose

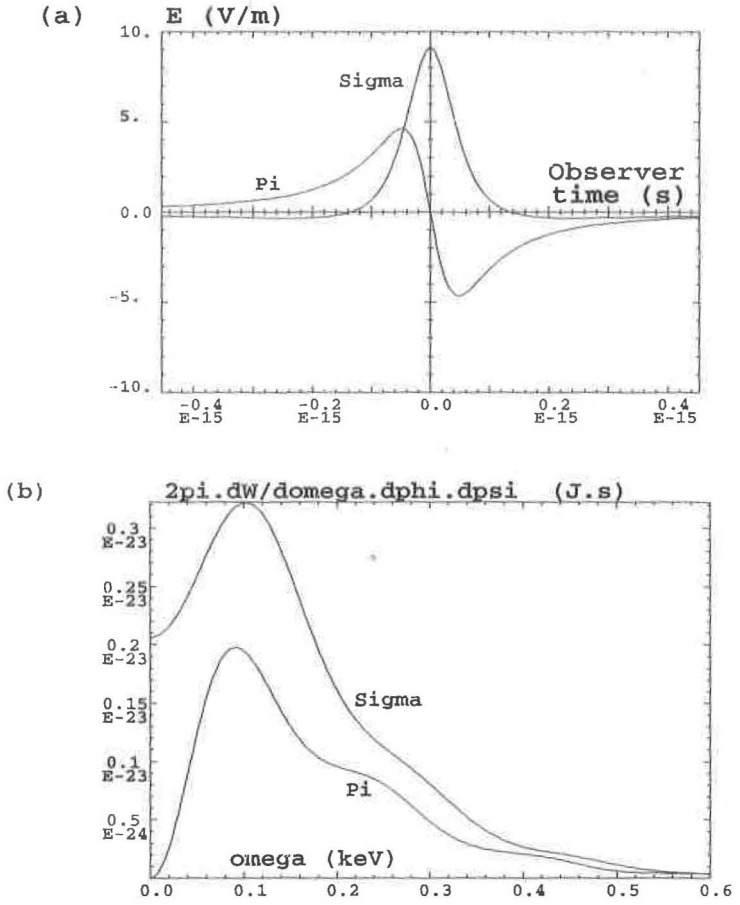

FIGURE 2 (a) Typical shapes of the $E_\sigma(t)$ and $E_\pi(t)$ SR components as observed in the direction of the centre of an $L \approx 20$ cm-long dipole, under (arbitrary) vertical aiming $\gamma\psi = 5$ (according to Eq. (12) for a 2.5 GeV electron on a $\rho = 53.6$ m circular trajectory, with $\phi = 0$ and observation distance $r = 10$ m). (b) The related spectral angular densities; the way they change form according to the truncature of $E(t)$ (i.e., according to the magnet length L) is addressed in Section 4.3 and Figure 8.

expressions are[10] (Figure 2)

$$E_\sigma(t) = \frac{((q\omega_0\gamma^4)/(\pi\epsilon_0 cr))(1 - 4\sinh^2(1/3A\sinh 2\overline{\omega}_c t))}{(1+\gamma^2\psi^2)^2[1+4\sinh^2(1/3A\sinh 2\overline{\omega}_c t)]^3},$$
$$E_\pi(t) = \frac{((q\omega_0\gamma^4)/(\pi\epsilon_0 cr))2\gamma\psi\sinh(1/3A\sinh 2\overline{\omega}_c t)}{(1+\gamma^2\psi^2)^{5/2}[1+4\sinh^2(1/3A\sinh 2\overline{\omega}_c t)]^3} \quad (12)$$

(with $\overline{\omega}_c = \omega_c/(1+\gamma^2\psi^2)^{3/2}$) differing from $E_{\sigma,\pi}(t')$ essentially by the squeeze of the central arch that ensues the $t(t')$ contraction (Eq. (6)). However these expressions have non-simple dependence on t which makes calculations easier to handle in t' variable.

The related spectra as obtained by numerical calculation of Eqs. (1) and (2) are shown in Figure 2(b) as expected the σ component does not go to zero with ω, due to the truncation of $E_\sigma(t)$ (Figure 2(a)) entailing $\int E_\sigma(t)\,dt \neq 0$ [a] in Eq. (4) whereas $\int E_\pi(t)\,dt$ stays null because $E_\pi(t)$ is odd. The left limit value in the spectra can be calculated from Eqs. (14).

In the classical hypothesis of an infinitely long dipole (that would lead to the $K_{2/3}^2$-, $K_{1/3}^2$-like σ and π spectra[8]) the electric field satisfies $\int E_{\sigma,\pi}(t)\,dt = 0$. Besides, given that $E_\sigma(t)$ is even, $\int E_\sigma(t)\,dt = 0$ tells that the area under the infinitely long negative tails equals that under the positive arch.

3.3 Spectral Angular Energy Density

Substituting Eqs. (10) into Eq. (5) and introducing the total deviation angle $\alpha = 2\omega_0 T'$ one gets the spectral amplitude density in the low frequency approximation ($\omega \ll 2\gamma^2 c/L(1+\gamma^2\alpha^2/12)$, Eq. (8))

$$\begin{aligned}
\tilde{E}_\sigma(\omega) &= \frac{q\gamma^2}{(2\pi)^{3/2}\epsilon_0 cr}\left[\frac{\alpha/2-\phi}{1+\gamma^2\psi^2+\gamma^2(\alpha/2-\phi)^2}\right. \\
&\quad \left. + \frac{\alpha/2+\phi}{1+\gamma^2\psi^2+\gamma^2(\alpha/2+\phi)^2}\right], \\
\tilde{E}_\pi(\omega) &= \frac{q\gamma^2}{(2\pi)^{3/2}\epsilon_0 cr}\psi\left[\frac{1}{1+\gamma^2\psi^2+\gamma^2(\alpha/2-\phi)^2}\right. \\
&\quad \left. - \frac{1}{1+\gamma^2\psi^2+\gamma^2(\alpha/2+\phi)^2}\right].
\end{aligned} \tag{13}$$

Substituting Eq. (13) in Eq. (1) gives the spectral angular energy density

$$\frac{\partial^2 W_\sigma}{\partial\omega\partial\Omega} = \frac{q^2\gamma^4}{4\pi^3\epsilon_0 c}\left[\frac{\alpha/2-\phi}{1+\gamma^2\psi^2+\gamma^2(\alpha/2-\phi)^2} + \frac{\alpha/2+\phi}{1+\gamma^2\psi^2+\gamma^2(\alpha/2+\phi)^2}\right]^2,$$

[a] Such so-called strange electromagnetic waves showing non-zero electric field integrals are addressed in Refs. [12,13].

$$\frac{\partial^2 W_\pi}{\partial\omega\partial\Omega} = \frac{q^2\gamma^4}{4\pi^3\epsilon_0 c} \times \psi^2\left[\frac{1}{1+\gamma^2\psi^2+\gamma^2(\alpha/2-\phi)^2} - \frac{1}{1+\gamma^2\psi^2+\gamma^2(\alpha/2+\phi)^2}\right]^2 \tag{14}$$

with $\partial\Omega = \partial\phi\partial\psi$. The parameter $\gamma\alpha/2 \equiv \gamma\omega_0 T'$ can be understood as the ratio $2cT'/(2\rho/\gamma)$ of the magnetic field extent to the critical trajectory arc length $2\rho/\gamma$ that corresponds to the central positive arch in $E_\sigma(t)$; many properties to be derived ahead show asymptotic behaviour related to that ratio. The distributions are illustrated in Figure 3 in the case of a 2.5 GeV electron traversing a $(20/\gamma)$-deviation dipole, for which the low frequency approximation (Eq. (8)) is valid as long as $\lambda \gg 2\pi\alpha^2 L/24$, e.g., $\lambda \gg 1\ \mu\text{m}$ given $L = 20\,\text{cm}$.

3D graphs similar to those shown in Figure 3 have been produced elsewhere by numerical means, e.g., in SR studies at the LEP mini-wiggler,[6] and as to the peaked edge SR, in the course of investigations on SR from straight sections at ESRF[11] and in relation with edge SR studies in Ref. [15]. These types of patterns have also recently been subject to experimental recording at LEP[6,16] and ESRF.[11]

As stressed above[b] (Eq. (4)), $\partial^2 W/\partial\omega\partial\Omega$ does not depend on the observation frequency ω in the low frequency approximation[c] (Eq. (8)) and in particular, $\int E_\sigma(t)\,dt \neq 0$ upon finite dipole length entails non-zero energy density for $\omega \to 0$ by contrast to the $K_{2/3}^2$ classical model, which benefits to the low frequency range.[d] Also, as expected from what precedes $\partial^2 W_\sigma/\partial\omega\partial\Omega$ reaches a maximum in the direction $\phi = 0$ for $\gamma\alpha = 2$ (Figure 6(a)) that is, for a $2/\gamma$ particle deviation when the sole positive arch in $E_\sigma(t)$ is intercepted – this is addressed in Section 4. From thereon, if $\gamma\alpha$ increases $\int E_\sigma(t)\,dt$ decreases since part of the negative tails in $E_\sigma(t)$ is intercepted by the observer, and correlatively the $\partial^2 W_\sigma/\partial\omega\partial\Omega$ maximum at $\phi = 0$ leaves the place to the depression between the two end peak pairs as shown in Figure 3(a). Conversely, if $\gamma\alpha$

[b] And in agreement with published experimental results.[17]

[c] Such is not the case for the high frequency part of the spectrum which extends according to the way $E(t)$ is truncated, i.e., according to the magnet length L; this is addressed in Section 4.3.

[d] In Refs. [5,6] this property was found to cause relatively higher intensity loss than predicted by the $K_{2/3}$ model, upon interference between short dipoles.

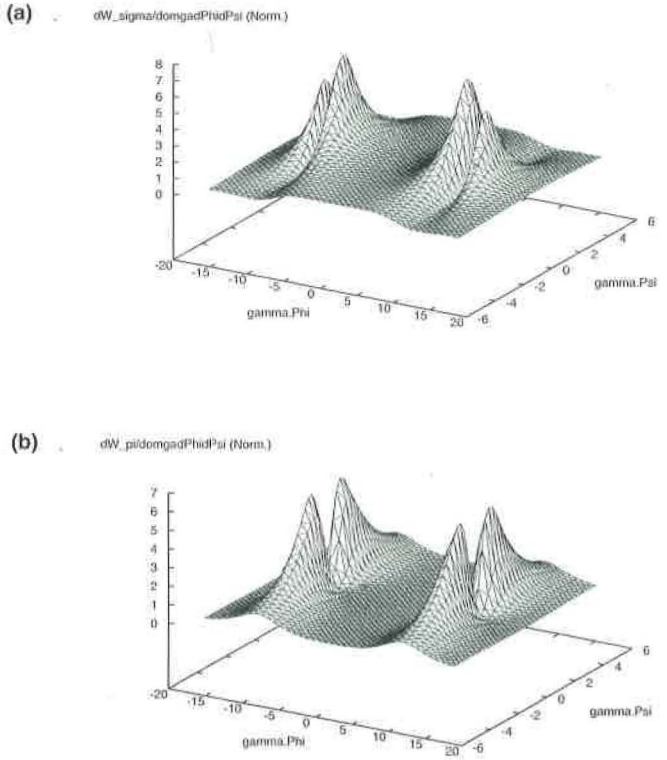

FIGURE 3 Angular distribution of the radiation emitted by a charge traversing an $\alpha \equiv (20/\gamma)$-deviation dipole (Eq. (14) with $\gamma\alpha = 20$): the graphs are normalised to the maximum of the σ radiation from the centre of the dipole (upper Eq. (14) with $\phi = \psi = 0$). The end peaks are due to edge SR: following Eq. (26) (with $\gamma\alpha \gg 1$) the σ component (a) is zero in observation directions $(\phi, \psi) = (\pm\alpha/2, 0)$ that is to say, when observing the dipole ends, and it is peaked in $\pm 1/\gamma$ directions on both sides of both dipole ends namely, at $(\phi, \psi) = (\pm(\alpha/2 \pm 1/\gamma), 0)$ (Eq. (27)); the end σ-peaks tend to equal amplitude as $\gamma\alpha$ increases. The π component (b) is peaked at dipole ends in the directions $(\phi, \psi) = (\pm\alpha/2, \pm 1/\gamma)$ (Eq. (25)); it is zero on the $\phi = 0$ and on the $\psi = 0$ axis.

decreases the $\phi = 0$ maximum persists, yet loses amplitude correlatively with the ensuing truncation of the $E_\sigma(t)$ positive arch. On the other hand $\partial^2 W_\pi / \partial\omega\partial\Omega$ does not strongly depend on $\gamma\alpha$; $\partial^2 W_\pi / \partial\omega\partial\Omega$ is zero on the $\psi = 0$ axis since $E_\pi(t)|_{\psi=0} \equiv 0$ (Eq. (10)), and is zero on the $\phi = 0$ axis since $\int E_\pi(t)\,\mathrm{d}t|_{\phi=0} \equiv 0$ (Eq. (13)), hence the four-lobe shape of the π spectral angular density (Figure 3(b)).

The projections of the spectral angular energy density onto the ϕ and ψ observation directions are obtained by integration of Eqs. (14)

so that, on the one hand as concerns the ϕ projection (Figure 4(a))

$$\begin{aligned}\frac{\partial^2 W_\sigma}{\partial\omega\partial\phi} &= \frac{q^2\gamma}{8\pi^2\epsilon_0 c}\left[\frac{\gamma^2(\alpha/2-\phi)^2}{(1+\gamma^2(\alpha/2-\phi)^2)^{3/2}}\right.\\ &\quad + \frac{\gamma^2(\alpha/2+\phi)^2}{(1+\gamma^2(\alpha/2+\phi)^2)^{3/2}} + 2\frac{(\alpha/2)^2-\phi^2}{\alpha\phi}\\ &\quad \left.\times\left(\frac{1}{\sqrt{1+\gamma^2(\alpha/2-\phi)^2}} - \frac{1}{\sqrt{1+\gamma^2(\alpha/2+\phi)^2}}\right)\right],\\ \frac{\partial^2 W_\pi}{\partial\omega\partial\phi} &= \frac{q^2\gamma}{8\pi^2\epsilon_0 c}\left[\frac{1}{\sqrt{1+\gamma^2(\alpha/2-\phi)^2}} + \frac{1}{\sqrt{1+\gamma^2(\alpha/2+\phi)^2}}\right.\\ &\quad \left.+ 2\frac{\sqrt{1+\gamma^2(\alpha/2-\phi)^2} - \sqrt{1+\gamma^2(\alpha/2+\phi)^2}}{\gamma\alpha\gamma\phi}\right],\end{aligned} \tag{15}$$

on the other hand as concerns the ψ projection (Figure 4(b))

$$\begin{aligned}\frac{\partial^2 W_\sigma}{\partial\omega\partial\psi} &= \frac{q^2\gamma}{4\pi^2\epsilon_0 c}\frac{\gamma^2(\alpha/2)^2}{\sqrt{1+\gamma^2\psi^2}(1+\gamma^2\psi^2+\gamma^2(\alpha/2)^2)},\\ \frac{\partial^2 W_\pi}{\partial\omega\partial\psi} &= \frac{q^2\gamma}{4\pi^2\epsilon_0 c}\gamma^2\psi^2\frac{\gamma^2(\alpha/2)^2}{(1+\gamma^2\psi^2)^{3/2}(1+\gamma^2\psi^2+\gamma^2(\alpha/2)^2)}.\end{aligned} \tag{16}$$

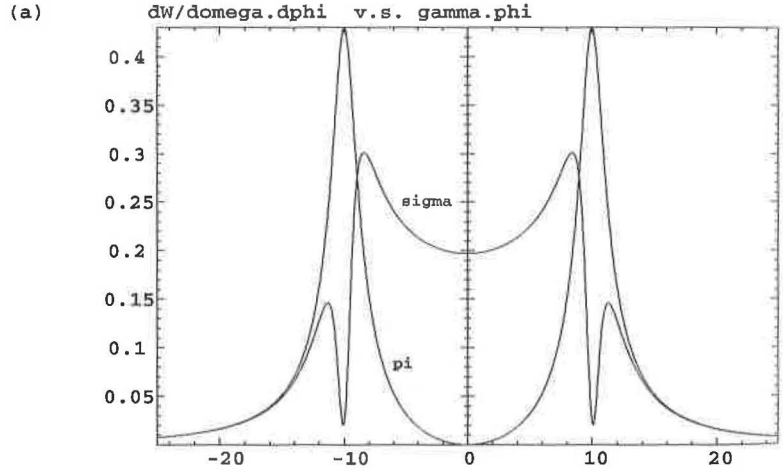

FIGURE 4(a)

(b)

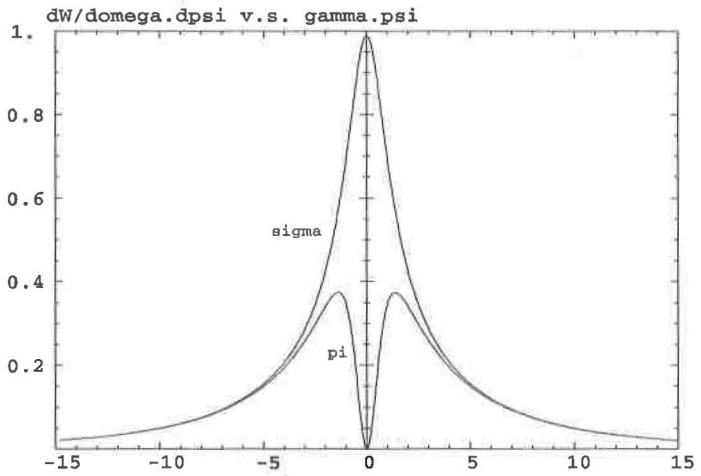

FIGURE 4(b)

FIGURE 4 Projections of the σ and π spectral angular densities of Figure 3 onto the ϕ and ψ observation directions (Eqs. (15) and (16)) with $\gamma\alpha = 20$). The graphs are normalised to the maximum of the ψ-projected σ amplitude issued from the centre of the dipole (upper Eq. (16) with $\psi = 0$).

Finally integration of the equations above gives the spectral energy density

$$\begin{aligned} \frac{\mathrm{d}W_\sigma}{\mathrm{d}\omega} &= \frac{q^2}{2\pi^2\epsilon_0 c}\gamma\alpha/2\frac{A\sinh(\gamma\alpha/2)}{\sqrt{1+(\gamma\alpha/2)^2}}, \\ \frac{\mathrm{d}W_\pi}{\mathrm{d}\omega} &= \frac{q^2}{2\pi^2\epsilon_0 c}\left(\frac{\sqrt{1+(\gamma\alpha/2)^2}}{\gamma\alpha/2}A\sinh(\gamma\alpha/2)-1\right). \end{aligned} \tag{17}$$

In the short dipole limit $\gamma\alpha \ll 1$ (i.e., when a small fraction of the positive arch of the electric field impulse is observed) one gets

$$\begin{aligned} \frac{\mathrm{d}W_\sigma}{\mathrm{d}\omega} &\xrightarrow{\gamma\alpha\ll 1} \frac{q^2\gamma}{8\pi^2\epsilon_0 c}\gamma^2\alpha^2 = 1.225\times 10^{-37}\gamma^2\alpha^2, \\ \frac{\mathrm{d}W_\pi}{\mathrm{d}\omega} &\xrightarrow{\gamma\alpha\ll 1} \frac{q^2\gamma}{24\pi^2\epsilon_0 c}\gamma^2\alpha^2 = 0.408\times 10^{-37}\gamma^2\alpha^2 \end{aligned} \tag{18}$$

and the partition is $(\mathrm{d}W_\sigma/\mathrm{d}\omega)/(\mathrm{d}W_\pi/\mathrm{d}\omega) = (3/4)/(1/4)$. The numerical values are for q = elementary charge and given in units of J s. The total

spectral density is the sum and writes

$$\frac{\mathrm{d}W}{\mathrm{d}\omega} = \frac{\mathrm{d}W_\sigma}{\mathrm{d}\omega} + \frac{\mathrm{d}W_\pi}{\mathrm{d}\omega} \overset{\gamma\alpha\ll 1}{\longrightarrow} \frac{q^2\gamma}{6\pi^2\epsilon_0 c}\gamma^2\alpha^2 = 1.633\times 10^{-37}\gamma^2\alpha^2. \quad (19)$$

In the long dipole limit $\gamma\alpha \gg 1$ (i.e., when the long negative tails in the observed electric field impulse have much wider extent than the sole central positive arch) one gets

$$\begin{aligned}
\frac{\mathrm{d}W_\sigma}{\mathrm{d}\omega} &\overset{\gamma\alpha\gg 1}{\longrightarrow} \frac{q^2}{2\pi^2\epsilon_0 c}\ln(\gamma\alpha) = 4.898\times 10^{-37}\ln(\gamma\alpha),\\
\frac{\mathrm{d}W_\pi}{\mathrm{d}\omega} &\overset{\gamma\alpha\gg 1}{\longrightarrow} \frac{q^2}{2\pi^2\epsilon_0 c}\ln\left(\frac{\gamma\alpha}{\mathrm{e}}\right) = 4.898\times 10^{-37}\ln\left(\frac{\gamma\alpha}{\mathrm{e}}\right),\\
\frac{\mathrm{d}W}{\mathrm{d}\omega} = \frac{\mathrm{d}W_\sigma}{\mathrm{d}\omega} + \frac{\mathrm{d}W_\pi}{\mathrm{d}\omega} &\overset{\gamma\alpha\gg 1}{\longrightarrow} \frac{q^2}{\pi^2\epsilon_0 c}\ln\left(\frac{\gamma\alpha}{\sqrt{\mathrm{e}}}\right) = 9.796\times 10^{-37}\ln\left(\frac{\gamma\alpha}{\sqrt{\mathrm{e}}}\right) \quad (20)
\end{aligned}$$

with $\mathrm{e}=\exp(1)$, and the ratio writes $(\mathrm{d}W_\sigma/\mathrm{d}\omega)/(\mathrm{d}W_\pi/\mathrm{d}\omega) = (\ln(\gamma\alpha))/(\ln(\gamma\alpha)-1)\approx(1/2)/(1/2)$. Equations (20) show that the spectral energy density is a logarithmically increasing function of $\gamma\alpha$ (within the model validity limit $\omega \ll 24c/\alpha^2 L$), i.e., of the ratio of the magnet length $L=\rho\alpha$ to the critical arc length $2\rho/\gamma$. In other words, the longer the negative tails in the electric field impulse (Figure 2(a)), the larger (logarithmically) the energy density in the low frequency range.

3.4 Radiation Opening

The horizontal and vertical rms opening angles for the σ component are

$$\begin{aligned}
\phi_{\sigma\text{-rms}} &= \frac{1}{\gamma}\left(\frac{\int_{-\infty}^{\infty}\gamma^2\phi^2\,(\partial^2 W_\sigma/\partial\omega\partial\Omega)\,\mathrm{d}(\gamma\phi)}{\int_{-\infty}^{\infty}(\partial^2 W_\sigma/\partial\omega\partial\Omega)\,\mathrm{d}(\gamma\phi)}\right)^{1/2}\\
&= \frac{1}{\gamma}\sqrt{1+\gamma^2\psi^2+(\gamma\alpha/2)^2},\\
\psi_{\sigma\text{-rms}} &= \frac{1}{\gamma}\left(\frac{\int_{-\infty}^{\infty}\gamma^2\psi^2\,(\partial^2 W_\sigma/\partial\omega\partial\Omega)\,\mathrm{d}(\gamma\psi)}{\int_{-\infty}^{\infty}(\partial^2 W_\sigma/\partial\omega\partial\Omega)\,\mathrm{d}(\gamma\psi)}\right)^{1/2}\\
&\overset{\phi\to 0}{\longrightarrow} \frac{1}{\gamma}\sqrt{1+(\gamma\alpha/2)^2}.
\end{aligned} \quad (21)$$

(The ϕ dependence of $\psi_{\sigma-\text{rms}}$ is a lengthy expression of little interest; hence we just show its $\phi\to 0$ limit.) The σ-opening is therefore a cone with rms aperture $\sqrt{1+(\gamma\alpha/2)^2}/\gamma$ and increases with magnet length

at given γ in the low frequency approximation (Eq. (8)). In the short dipole limit and under $\psi = 0$ aiming one gets

$$\phi_{\sigma\text{-rms}} \quad \text{and} \quad \psi_{\sigma\text{-rms}} \overset{\gamma\alpha \ll 1}{\longrightarrow} 1/\gamma \tag{22}$$

as expected.[18] In the long dipole limit (yet within the limit of the low frequency assumption $\omega \ll 24c/\alpha^2 L$) one gets

$$\phi_{\sigma\text{-rms}} \quad \text{and} \quad \psi_{\sigma\text{-rms}} \overset{\gamma\alpha \gg 1}{\longrightarrow} \alpha/2 \tag{23}$$

that is, both the horizontal and the vertical openings tend to half the value of the particle sweep angle α (see Figure 4). As to the π component, similar calculations provide identical dependence in $\gamma\alpha$ and identical asymptotic behaviour, namely

$$\phi_{\pi\text{-rms}} \overset{\psi \to 0}{\longrightarrow} \frac{1}{\gamma}\sqrt{1 + (\gamma\alpha/2)^2}, \qquad \psi_{\pi\text{-rms}} \overset{\phi \to 0}{\longrightarrow} \frac{1}{\gamma}\sqrt{1 + (\gamma\alpha/2)^2}. \tag{24}$$

One can observe (Figure 3) that the π component is peaked in, and confined around four directions obtainable from Eq. (13) by taking $\partial \tilde{E}_\pi/\partial\phi = 0$ and $\partial \tilde{E}_\pi/\partial\psi = 0$, namely

$$\phi_{\pi\text{-peak}} = \pm\frac{1}{\gamma}\frac{1 + (\gamma\alpha/2)^2}{\sqrt{2 + (\gamma\alpha/2)^2}}, \qquad \psi_{\pi\text{-peak}} = \pm\frac{1}{\gamma}\sqrt{\frac{1 + (\gamma\alpha/2)^2}{2 + (\gamma\alpha/2)^2}} \tag{25}$$

which are increasing functions of the magnet deviation α. For a short dipole one gets $\phi_{\pi\text{-rms}}, \psi_{\pi\text{-rms}} \to \pm 1/\gamma$ and $\phi_{\pi\text{-peak}}, \psi_{\pi\text{-peak}} \to \pm 1/\gamma\sqrt{2}$. For a long dipole one gets $\phi_{\pi\text{-rms}}, \psi_{\pi\text{-rms}} \to \pm\alpha/2$ and $\phi_{\pi\text{-peak}} \to \pm\alpha/2$ (which corresponds to the magnet ends) while $\psi_{\pi\text{-peak}} \to \pm 1/\gamma$.

3.5 Comments on Low Frequency Edge Radiation

Special SR properties such as edge radiation[2–4,14,15] (and in particular its enhanced low frequency energy density), transition radiation[19,20] can be understood in terms of the way the electric field impulse is truncated from the observer standpoint, which depends on the horizontal component ϕ of the observation direction (Eq. (10)), as schemed in Figure 5.

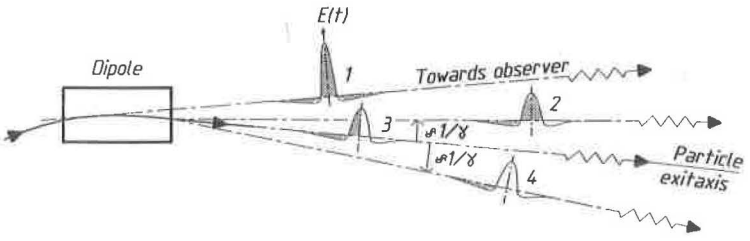

FIGURE 5 The shadowed areas materialise the various shapes of the $E_\sigma(t)$ polarisation component of the electric field impulse, as radiated over the all-dipole extent, from the observer viewpoint (according to Eq. (10)). The vertical component ψ of the observation angle has arbitrary value and the horizontal component ϕ is, graph 1: towards the body of the dipole; graph 2: $\sqrt{1+\gamma^2\psi^2}/\gamma$ upstream from the exit direction of the particle – main contribution to the edge radiation, the right negative tail is no longer seen; graph 3: in the exit direction – only half the impulse is seen, the field integral is almost zero; graph 4: $\sqrt{1+\gamma^2\psi^2}/\gamma$ downstream of the exit direction – second contribution to edge SR, only the left negative tail remains in sight.

In a particular direction close to the particle trajectory incidence at magnet ends the low frequency spectral angular density in the σ component is zero; this is when $E_\sigma(t)$ is truncated in the vicinity of its symmetry axis in such a way that the area under the positive half-arch equals that under the negative tail (graph 3 in Figure 5). The exact direction depends on $\gamma\alpha$ that is to say, on the dipole length $L = 2cT'$ or equivalently on the impulse width $2\tau_c = 2(1+\gamma^2\psi^2)^{3/2}/\omega_c$; it can be obtained from Eq. (13) by solving $\tilde{E}_\sigma(\omega) = 0$ for ϕ, which gives

$$\phi_{\sigma\text{-zero}} = \pm\frac{1}{\gamma}\sqrt{1+\gamma^2\psi^2+(\gamma\alpha/2)^2}. \tag{26}$$

Upon $\psi = 0$ aiming one gets $\phi_{\sigma\text{-zero}} = \sqrt{1+(\gamma\alpha/2)^2}/\gamma$ and, for large values of $\gamma\alpha$ (i.e., long negative tails) $\phi_{\sigma\text{-zero}} \to \pm\alpha/2$ and identifies with the particle direction at magnet ends, that is to say, there is no radiation from magnet ends!

At angles very close to the particle incidence at dipole ends the time integral $\int E_\sigma(t')\,dt'$ is extremum: maximum towards the body of the magnet (graph 2 in Figure 5), relative maximum outwards (graph 4 in Figure 5), while $\int E_\pi(t')\,dt'$ reaches about $\frac{1}{4}$ of the (maximum) value attained when observing in the exit direction of the particle; these are the two incidences under which edge SR happens to deliver spectral angular

energy density noticeably stronger than regular SR originating from the magnet body. Those angles can be obtained by solving $\partial \bar{E}_\sigma(\omega)/\partial\phi = 0$ for ϕ (Eq. (13)), which leads to

$$\phi_{\sigma\text{-peak}} = \pm\frac{1}{\gamma}\sqrt{1+\gamma^2\psi^2+(\gamma\alpha/2)^2 \pm 2\sqrt{1+\gamma^2\psi^2}\sqrt{1+\gamma^2\psi^2+(\gamma\alpha/2)^2}}$$
$$\overset{\psi\to 0}{\longrightarrow} \pm\frac{1}{\gamma}\sqrt{1+(\gamma\alpha/2)^2 \pm 2\sqrt{1+(\gamma\alpha/2)^2}} \overset{\gamma\alpha\gg 1}{\longrightarrow} \pm\left(\alpha/2 \pm \frac{1}{\gamma}\right). \quad (27)$$

In other words in very long dipoles ($\gamma\alpha \gg 1$) the energy density is peaked in directions $\pm 1/\gamma$ on each side of dipole ends as expected,[14,15] while in shorter magnets the position of the peaks depends on the magnet length (through $\gamma\alpha$). The peak amplitudes are obtained from Eq. (14) with $\psi = 0$ and, respectively for the low and high amplitude one, in the long dipole limit, $\phi \doteq \pm(\alpha/2 + 1/\gamma)$, $\phi = \pm(\alpha/2 - 1/\gamma)$ (Eq. (27)) which leads to the energy ratio

$$\frac{\partial^2 W_{\sigma,\text{low-peak}}}{\partial\omega\partial\Omega} : \frac{\partial^2 W_{\sigma,\text{high-peak}}}{\partial\omega\partial\Omega} = \left(1-\frac{1}{\gamma\alpha/2}\right)^2 : \left(1+\frac{1}{\gamma\alpha/2}\right)^2$$
$$\overset{\gamma\alpha/2\gg 1}{\longrightarrow} 1:1. \quad (28)$$

The low and high peaks tend to reach identical amplitude as $\gamma\alpha$ increases: this is because the energy brought to the low peak by the negative tail in $E_\sigma(t)$ tends to match that brought to the high peak by the positive arch.

The π component is zero on the $\phi = 0$ and $\psi = 0$ axis due to $\tilde{E}_\pi\,|_{\phi=0} \equiv 0$ and $\tilde{E}_\pi\,|_{\psi=0} \equiv 0$ (Eq. (13)). On the other hand the π component is peaked in the directions ($\phi_{\pi\text{-peak}}$, $\psi_{\pi\text{-peak}}$) defined in Eq. (25).

Figure 3 shows the typical shape and the above features of the angular distribution of low frequency edge radiation in a $(20/\gamma)$-deviation dipole. The σ-component edge peak amplitude (Figure 3(a)) is 7.8 times larger than the peak energy density issued from the centre of the body (yet they still are 3.3 times weaker than the enhanced low frequency radiation from a stand-alone $(2/\gamma)$-dipole, as shown in Section 4.4).

4 ENHANCED LOW FREQUENCY ENERGY DENSITY

From what precedes it appears that the low frequency energy density is maximised upon truncating the E_σ impulse at $\pm\tau_c$. Doing so isolates the central positive arch of the impulse and maximises the integral $\int E_\sigma(t)\,dt$ and hence the intensity in the σ component, in the low frequency spectral range. This is achieved by observing the centre of a $(2/\gamma)$-deviation dipole; as shown below the gain on the spectral angular energy density so obtained w.r.t. body SR from a long dipole reaches orders of magnitude in the low frequency range, this last being determined by[e] (Eq. (8) with $\gamma\alpha = 2$), $\omega \ll 3\gamma^2 c/2L = 3\gamma^3 c/4\rho = \omega_c/2$.

4.1 Parameters of a $(2/\gamma)$-Dipole

The deviation in the dipole satisfies $BL/B\rho = 2/\gamma$. Taking $B\rho = p/q \simeq E/c = \gamma E_0/c$ (with E = particle energy and E_0 = rest energy) this fixes the magnetic field integral, namely (B in Tesla, L in meter)

$$BL = 2E_0/c \approx 1/300 \text{ (T m)} \quad \text{(for electrons)}. \tag{29}$$

Typically $L \approx$ centimeters and $B \approx$ kGauss; for instance, taking $L = 2.15$ cm in Eq. (29) entails $B = 0.155$ T, independent of particle energy. In a 2.5 GeV machine this means a 0.41 mrad orbit deviation. The rect($t'/2T'$) field model (Eq. (10)) remains valid as long as the magnet gap is much smaller than its length. In relation with the low frequency criterion $\omega \ll 3\gamma^2 c/2L$ which determines the frequency validity domain, that could be a convenient criterion in order to fix a lower limit to L, given the vacuum pipe diameter, so as to preserve the validity of the analytical formalism developed so far.

4.2 Properties of the Low Frequency Radiation

The spectral angular energy density writes (Eq. (14) with $\gamma\alpha = 2$) (Figure 6)

$$\frac{\partial^2 W_\sigma}{\partial\omega\partial\Omega}(\omega \ll \omega_c/2) = \frac{q^2\gamma^2}{\pi^3\epsilon_0 c}\left(\frac{2 - \gamma^2\phi^2 + \gamma^2\psi^2}{4(1 + \gamma^2\psi^2) + (\gamma^2\phi^2 + \gamma^2\psi^2)^2}\right)^2,$$

[e] Note that, the smaller L, the wider the low frequency approximation range. For instance, one gets $\omega \ll 10^{16}/L$ (rad/s) ($\lambda \gg 0.2 \times 10^{-6} L$ (m)) at 2.5 GeV, $\omega \ll 4 \times 10^{18}/L$ (rad/s) ($\lambda \gg 5 \times 10^{-10} L$ (m)) at 45 GeV.

(a) dW_sigma/domgadPhidPsi (Norm.)

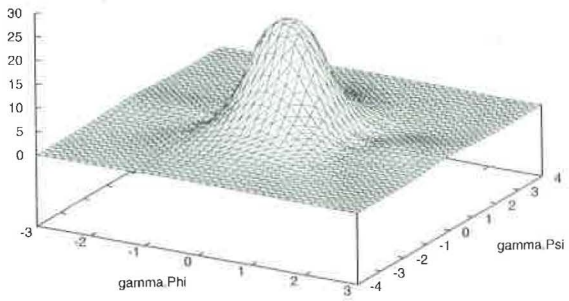

(b) dW_pi/domgadPhidPsi (Norm.)

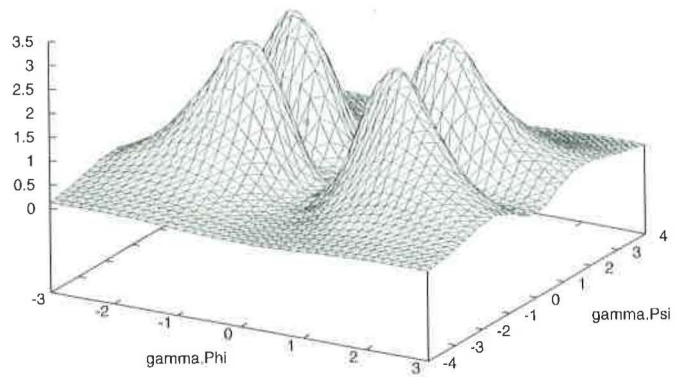

FIGURE 6 Angular density $\partial^3 W/\partial\omega\partial\phi\partial\psi$ from a $(2/\gamma)$-deviation dipole (Eq. (30)). The graphs are normalised as in Figure 3 in order to allow comparison. (a) σ component, peaked at $(\phi, \psi) = (0, 0)$ and at the two weak side lobes in the directions

$$(\phi, \psi) = (\pm\sqrt{2}\sqrt{1+\sqrt{2}}/\gamma,\ 0)$$

(Eq. (27) with $\gamma\alpha = 2$); the depressions in between are at $(\pm\sqrt{2}/\gamma, 0)$ (Eq. (26)). (b) π component; its intensity is zero along the ϕ and $\psi = 0$ directions; it is peaked in the four directions $(\phi, \psi) = (\pm 2/\gamma\sqrt{3},\ \pm\sqrt{2}/\gamma\sqrt{3})$ (Eq. (25)).

$$\frac{\partial^2 W_\pi}{\partial\omega\partial\Omega}(\omega \ll \omega_c/2) = \frac{q^2\gamma^2}{\pi^3\epsilon_0 c}\left(\frac{2\gamma\phi\gamma\psi}{4(1+\gamma^2\psi^2)+(\gamma^2\phi^2+\gamma^2\psi^2)^2}\right)^2. \tag{30}$$

By comparing Figures 3(a) and 6(a) it can be observed that the two weak outward side lobes of the σ component edge SR are damped to

almost negligible amplitude (obtainable from Eq. (14) with $\psi = 0$ and (after Eq. (27)) $\phi = \pm\sqrt{2}\sqrt{1+\sqrt{2}}/\gamma$), while the two inward lobes merge into a unique central one. The projections write (Eqs. (15) and (16)) (Figure 7)

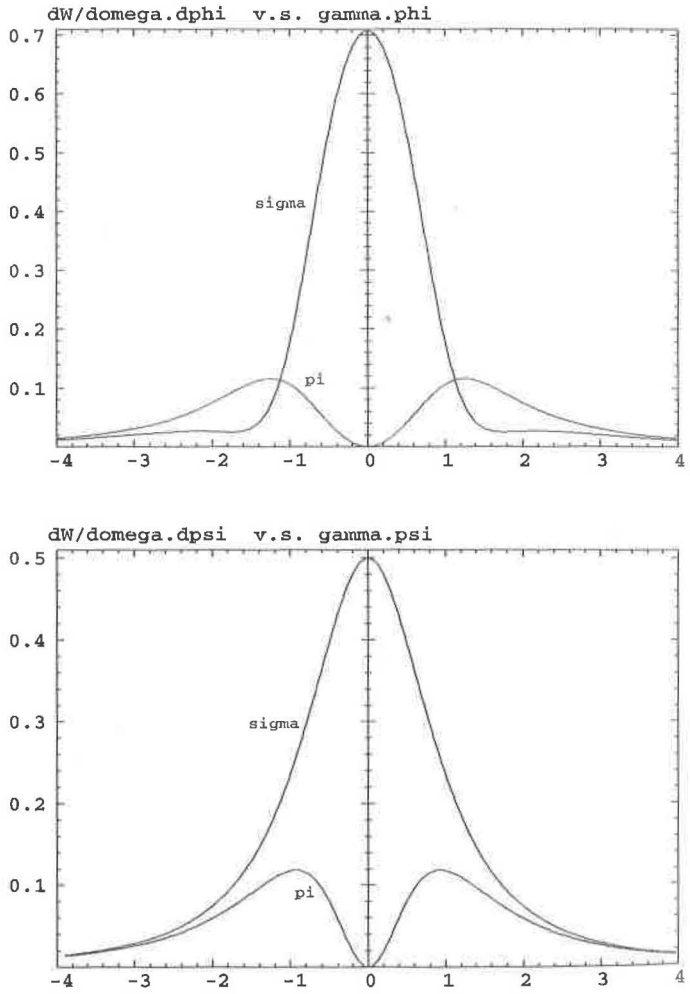

FIGURE 7 Projections of the σ and π spectral angular densities from a $(2/\gamma)$-dipole onto the ϕ and ψ observation directions (Eqs. (31)). The graphs are normalised as in Figure 4 to allow comparison.

$$\frac{\partial^2 W_\sigma}{\partial\omega\partial\phi} = \frac{q^2\gamma}{8\pi^2\epsilon_0 c}\left\{\frac{(1-\gamma\phi)^2}{(1+(1-\gamma\phi)^2)^{3/2}} + \frac{(1+\gamma\phi)^2}{(1+(1+\gamma\phi)^2)^{3/2}} + \frac{1-\gamma^2\phi^2}{\gamma\phi}\left[\frac{1}{\sqrt{1+(1-\gamma\phi)^2}} - \frac{1}{\sqrt{1+(1+\gamma\phi)^2}}\right]\right\},$$

$$\frac{\partial^2 W_\pi}{\partial\omega\partial\phi} = \frac{q^2\gamma}{8\pi^2\epsilon_0 c}\left[\frac{1}{\sqrt{1+(1-\gamma\phi)^2}} + \frac{1}{\sqrt{1+(1+\gamma\phi)^2}} + \frac{\sqrt{1+(1-\gamma\phi)^2} - \sqrt{1+(1+\gamma\phi)^2}}{\gamma\phi}\right], \tag{31}$$

$$\frac{\partial^2 W_\sigma}{\partial\omega\partial\psi} = \frac{q^2\gamma}{2\pi^2\epsilon_0 c}\frac{1}{\sqrt{1+\gamma^2\psi^2}(2+\gamma^2\psi^2)},$$

$$\frac{\partial^2 W_\pi}{\partial\omega\partial\psi} = \frac{q^2\gamma}{2\pi^2\epsilon_0 c}\gamma^2\psi^2\frac{1}{(1+\gamma^2\psi^2)^{3/2}(2+\gamma^2\psi^2)}.$$

The spectral energy density writes (Eq. (17))

$$\frac{\mathrm{d}W_\sigma}{\mathrm{d}\omega} = \frac{q^2}{2\sqrt{2}\pi^2\epsilon_0 c}A\sinh(1) = 3.053\times10^{-37}\quad(\mathrm{J\,s}),$$
$$\frac{\mathrm{d}W_\pi}{\mathrm{d}\omega} = \frac{q^2}{2\pi^2\epsilon_0 c}\left(\sqrt{2}\,A\sinh(1)-1\right) = 1.207\times10^{-37}\quad(\mathrm{J\,s}) \tag{32}$$

where the numerical values hold for q = elementary charge. One therefore gets the partition $(\mathrm{d}W_\sigma/\mathrm{d}\omega)/(\mathrm{d}W_\pi/\mathrm{d}\omega) = 2.53$.

The rms openings and π-peak directions are (Eqs. (21), (24) and (25) with $\gamma\alpha = 2$)

$$\phi_{\sigma\text{-rms}} = \psi_{\sigma\text{-rms}} = \phi_{\pi\text{-rms}} = \psi_{\pi\text{-rms}} = \sqrt{2}/\gamma,$$
$$\phi_{\pi\text{-peak}} = \pm 2/\gamma\sqrt{3},\quad \psi_{\pi\text{-peak}} = \pm\sqrt{2}/\gamma\sqrt{3}. \tag{33}$$

These properties stay unchanged at constant γ, that is, at constant deviation $2/\gamma$ or equivalently at constant field integral BL (Figure 8(a)). The spectral angular energy density in the low frequency range decreases when the dipole deviation departs from $2/\gamma$ (Figure 8(b)), its projections (Eqs. (31)) decrease as well, whether the deviation decreases (this is because the positive arch of the electric field impulse received by the observer is truncated within $\pm\tau_c$) or whether the deviation increases (this is because part of the negative tails are introduced in the electric field impulse received by the observer during a time $t > 2\tau_c$, which is detrimental to $\int E_\sigma\,\mathrm{d}t$ and hence to low frequency radiation);

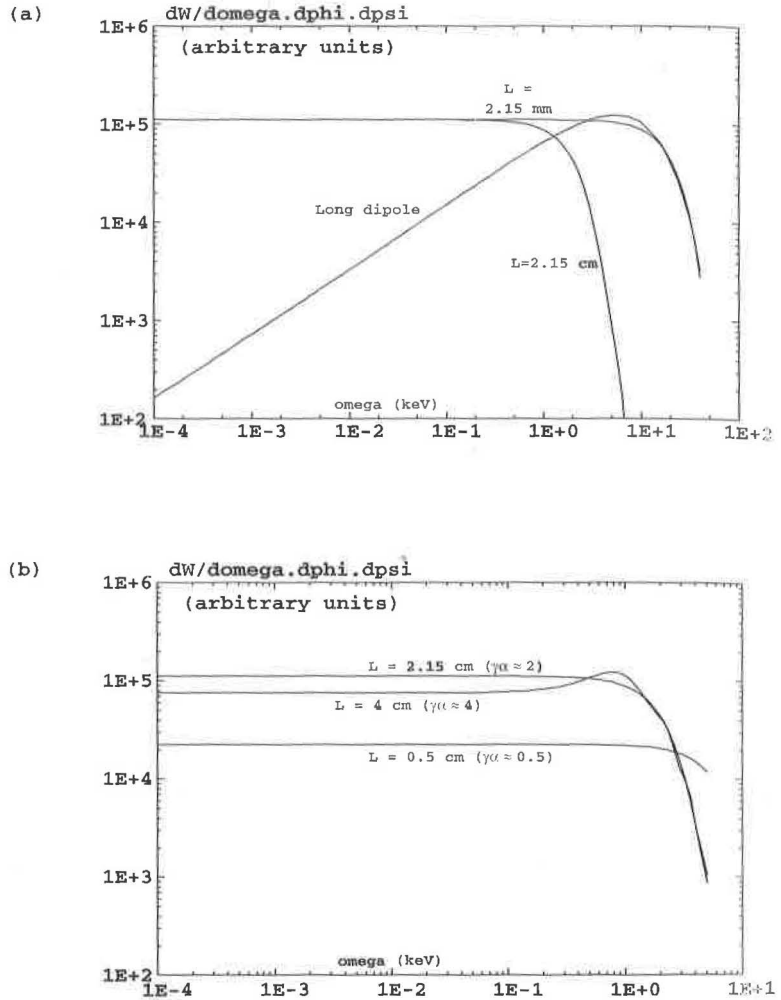

FIGURE 8 Energy density in the forward direction ($\phi=\psi=0$), as obtained from numerical calculation of Eqs. (1) and (2) (constant over frequency range as stated in Eq. (8)). (a) the graph compares the $K_{2/3}^2$-like spectrum from a 2.5 GeV electron in field $B=1.55\,\mathrm{T}$ ($\rho=5.4\,\mathrm{m}$), and the σ-spectrum from a $(2/\gamma)$-dipole with field integral $BL=1/300\,\mathrm{T\,m}$, in two cases: the dipole is either a $(2\rho/\gamma)$-long piece of the former, with length $L=1/300\,B=2.15\,\mathrm{mm}$ (Eq. (29)), or the dipole length is ten times longer with ten times weaker field; both these $(2/\gamma)$-dipoles provide identical and maximum energy density (Eq. (30)) in the low frequency range ($\omega\ll\omega_c/2$), more than 100 times that from the long dipole if $\omega<1.2\,\mathrm{eV}$ ($\lambda>1\,\mu\mathrm{m}$) (Eq. (37)). (b) starting from $(2/\gamma)$ deviation ($L=2.15\,\mathrm{cm}$), the field integral is varied by changing L at constant B: the graph shows that $\partial^2 W_\sigma/\partial\omega\partial\Omega|_{\phi=\psi=0}$ in the low frequency region (Eq. (30)) decreases when BL departs from $1/300\,\mathrm{T\,m}$ (Eq. (29)).

the latter effect is accompanied by an increase of the radiation opening with an overall effect of about constant integrated power per unit of magnet length.

4.3 Comparison with Classical SR Model

The properties of low frequency SR in a finite extent magnetic field as described above sensibly depart from what the classical theory of low frequency SR from an infinitely long dipole provides. Let us write the latter under the form (after Ref. [8])

$$\begin{aligned}\frac{\partial^2 W_\sigma}{\partial\omega\partial\Omega} &= \frac{3q^2\gamma^2}{8\pi^3\epsilon_0 c}\frac{\Gamma(2/3)^2}{2^{1/3}}\left(\frac{\omega}{\omega_c}\right)^{2/3} = 1.70\times 10^{-37}\gamma^2\left(\frac{\omega}{\omega_c}\right)^{2/3},\\ \frac{\partial^2 W_\pi}{\partial\omega\partial\Omega} &= \frac{3q^2\gamma^2}{16\pi^3\epsilon_0 c}\frac{\Gamma(1/3)^2}{2^{2/3}}\gamma^2\psi^2\left(\frac{\omega}{\omega_c}\right)^{4/3}\\ &= 2.64\times 10^{-37}\gamma^2(\gamma\psi)^2\left(\frac{\omega}{\omega_c}\right)^{4/3}\end{aligned} \tag{34}$$

and with γ-independent vertical rms opening angles[8]

$$\psi_{\sigma,R} = 0.7560(\omega_0/\omega)^{1/3}, \qquad \psi_{\pi,R} = 1.0143(\omega_0/\omega)^{1/3} \tag{35}$$

much larger than $1/\gamma$ and increasing with decreasing observation frequency ω.

On the other hand, taking Eq. (30) with $\phi = 0$ gives the σ spectral angular energy density from a $(2/\gamma)$-dipole in the low frequency approximation in the forward direction (the π density is zero in the forward direction)

$$\left.\frac{\partial^2 W_\sigma}{\partial\omega\partial\Omega}\right|_{\phi=0} = \frac{q^2\gamma^2}{\pi^3\epsilon_0 c}\frac{1}{(2+\gamma^2\psi^2)^2} \approx 3.12\times 10^{-37}\frac{\gamma^2}{(2+\gamma^2\psi^2)^2}. \tag{36}$$

Comparing Eqs. (36) and (34) leads to the energy ratio in the bend plane ($\psi = 0$)

$$\begin{aligned}&\left.\frac{\partial^2 W_\sigma}{\partial\omega\partial\Omega}\right|_{\text{Classical}} : \left.\frac{\partial^2 W_\sigma}{\partial\omega\partial\Omega}\right|_{(2/\gamma)\text{-dipole}}\\ &\quad = \frac{3\,\Gamma(2/3)^2}{2^{4/3}}\left(\frac{\omega}{\omega_c}\right)^{2/3} : 1\end{aligned} \tag{37}$$

possibly highly in favour of the $(2/\gamma)$-dipole. Namely, taking $\rho = 5\,\text{m}$, $\omega = 1.88\times 10^{15}\,\text{rad s}^{-1}$ ($\lambda = 1\,\mu\text{m}$) in Eq. (34), one gets, for $E = 2.5\,\text{GeV}$,

$\omega/\omega_c \approx 1.8 \times 10^{-4}$ and the ensuing ratio $\partial^2 W_\sigma/\partial\omega\partial\Omega|_{\text{Classical}} : \partial^2 W_\sigma/\partial\omega\partial\Omega|_{(2/\gamma)\text{-dipole}} \approx 1:140$ (Figure 8(a)).

As to the openings, the $(2/\gamma)$-dipole SR is confined in a cone with $\sqrt{2}/\gamma$ rms aperture (Eq. (33)) independent of ω, while that of the long dipole is much wider, namely, $\gamma\phi_R \approx \gamma\alpha/2 \approx \text{mrad} \times \gamma$ in the bend plane and (Eq. (35) with the numerical values above) $\gamma\psi_R \approx 10$ proportional to $\gamma\omega^{1/3}$ in the vertical plane.

Figure 8(a) more generally compares the spectral angular energy density in the forward direction ($\phi = \psi = 0$), over the all-effective spectral range of the radiation (obtained by numerical computation). It can be checked that the $(2/\gamma)$-dipole energy density in the low frequency range does not depend on its length contrary to what occurs at high frequency (the shorter the $(2/\gamma)$-dipole, the wider the spectrum extent). In particular an adequately short $(2/\gamma)$-dipole appears to deliver high frequency spectral energy density asymptotically comparable to that from a long dipole.

Another way to compare long and short dipole radiation *within the low frequency approximation* (Eq. (8)) is as follows. The peak σ spectral angular energy density for both is obtained from Eq. (14) taken for $\psi = 0$, namely

$$\frac{\partial^2 W_\sigma}{\partial\omega\partial\Omega} = \frac{q^2\gamma^4}{4\pi^3\epsilon_0 c}\left[\frac{\alpha/2-\phi}{1+\gamma^2(\alpha/2-\phi)^2} + \frac{\alpha/2+\phi}{1+\gamma^2(\alpha/2+\phi)^2}\right]^2. \tag{38}$$

The peak energy density from the long dipole body ensues by substituting $\phi = 0$ and taking $\gamma\alpha \gg 1$ in Eq. (38), and the peak $(2/\gamma)$-dipole energy density is obtained by substituting $\phi = 0$ and $\gamma\alpha = 2$, which we write

$$\left.\frac{\partial^2 W_\sigma}{\partial\omega\partial\Omega}\right|_{\text{Long-dipole}} = \frac{q^2\gamma^2}{\pi^3\epsilon_0 c}\frac{1}{(\gamma\alpha/2)^2} \quad \text{and} \quad \left.\frac{\partial^2 W_\sigma}{\partial\omega\partial\Omega}\right|_{(2/\gamma)\text{-dipole}} = \frac{q^2\gamma^2}{4\pi^3\epsilon_0 c}. \tag{39}$$

Their ratio writes

$$\left.\frac{\partial^2 W_\sigma}{\partial\omega\partial\Omega}\right|_{\text{Long-dipole}} : \left.\frac{\partial^2 W_\sigma}{\partial\omega\partial\Omega}\right|_{(2/\gamma)\text{-dipole}} = \left(\frac{1}{\gamma\alpha/2}\right)^2 : \frac{1}{4} = 1 : (\gamma\alpha/4)^2 \tag{40}$$

and diverges with increasing $\gamma\alpha$ (the Long-dipole body SR tends to zero). For instance, for $\gamma\alpha \approx 20$ (e.g., 22 cm long dipole with magnetic field 0.155 T at 2.5 GeV, validity range (Eq. (8)) $\lambda \gg \alpha^2 L/24 \approx 10^{-6}$ m) the ratio is 1 : 100; for $\gamma\alpha \approx 50$ (e.g., 50 cm long dipole with magnetic field 0.155 T at 45 GeV, $\lambda \gg 0.04 \times 10^{-6}$ m) a 1 : 150 ratio comes out.

4.4 Comparison with Edge SR

The gain in σ energy density from a $(2/\gamma)$-dipole w.r.t edge radiation can be estimated from the shape of the observed electric field impulse, as follows. In the case of the $(2/\gamma)$-dipole the full positive arch of the σ impulse is received by the observer. In the case of the peak edge radiation (in the direction $1/\gamma$ from the magnet end – graph 2 in Figure 5) the observer receives in addition a part of the negative tail of that impulse. Following the Fourier transform approximation of Eq. (4) the energy density ratio [Edge : $(2/\gamma)$-dipole] is the square of the ratio of the electric field integrals, that is to say, 1 : 4 if the edge radiation is issued from an infinitely long dipole, a bit more if the dipole is not very long (since in such case, the negative tail of the edge electric field impulse is truncated – just like in Figure 5, and hence the area under $E_\sigma(t)$ is a little more than half the area under the sole positive arch).

This can be checked analytically. The ratio of the edge radiation peak energy density (Eq. (28)) to the $(2/\gamma)$-dipole peak energy density (Eq. (39)) writes

$$\left.\frac{\partial^2 W_\sigma}{\partial\omega\partial\Omega}\right|_{\text{Edge}} : \left.\frac{\partial^2 W_\sigma}{\partial\omega\partial\Omega}\right|_{(2/\gamma)\text{-dipole}} = \left(1+\frac{2}{\gamma\alpha}\right)^2 : 4 \overset{\gamma\alpha\gg 1}{\longrightarrow} 1:4. \tag{41}$$

Instead, for not too large $\gamma\alpha$ value one gets slightly increased edge SR. For instance, with $\alpha = 20/\gamma$ deviation one gets $(1+(1/10))^2 : 4 \approx 1 : 3.3$.

5 CONCLUSION

A simple theory of low frequency, far-field synchrotron radiation is established on the basis of the approximation of the radiated electric field Fourier transform by its time integral.

Special properties of low frequency SR are pointed out, and interpreted in terms of the shape and truncation of the electric field impulse. It is in particular shown that the spectral angular energy density takes its maximum at low frequency rather than in the ω_c critical frequency region as in the case of a long dipole. The method allows detailed comparison between edge and dipole body radiation.

As an application it is shown that a short, $(2/\gamma)$-deviation dipole causes the low frequency spectral angular energy density to be maximised, confined within a $\sqrt{2}/\gamma$ rms aperture cone, entailing a gain of up to four w.r.t. edge SR and up to several orders of magnitude w.r.t. body SR from a long dipole, and making it a highly recommendable candidate as a long-wavelength radiation source. Properties of the $(2/\gamma)$-dipole are derived and illustrated with numerical examples.

Acknowledgements

I am thankful to the Super-ACO/SOLEIL team (LURE and SOLEIL, Orsay) and O. Chubar (ESRF) for encouraging discussions, and to A. Hofmann and K. Hanke (CERN) for reading the manuscript.

References

[1] SOLEIL Laboratory CEA & CNRS, Gif sur Yvette, France; see for instance, *Proc. PAC Conf.*, Vancouver, Canada, 1997; and *Proc. EPAC Conf.*, Sitges, Spain, 1996.
[2] R. Coisson, On synchrotron radiation in non-uniform magnetic fields, *Optics Comm.*, **22**(2) (1977) 135–137.
[3] J. Bosser, L. Burnod, R. Coisson, G. Ferioli, J. Mann et and F. Méot, Characteristics of the radiation emitted by protons and antiprotons in an undulator, *J. Phys. Lett.*, **45** (1984) L-343–L-351.
[4] R. Coisson, Some possible effects modifying the far infrared synchrotron radiation spectrum, *J. Phys.-Lettres*, **45** (1984) L-89–L-94.
[5] F. Méot, Synchrotron radiation interferences at the LEP mini-wiggler, Report CERN SL/94-22 (AP), 28 June 1994.
[6] C. Bovet, A. Burns, F. Méot, M. Placidi, E. Rossa and J. de Vries, Synchrotron radiation interferences between short dipoles at LEP, Report CERN SL/97-59 (BI), 24 November 1997; and *Proc. PAC Conf.*, Vancouver, Canada, May 1997.
[7] K. Hanke, Measurement of the bunch length of LEP with a streak camera [...], Report PITHA 94/1, RWTH Aachen, May 1994; and CERN SL/Note 95-65 (BI), 13/06/1995.
[8] A. Hofmann, Theory of synchrotron radiation, SSRL ACD-Note 38, September 1986.
[9] R.A. Bosch and O. Chubar, Long wavelength edge radiation in an electron storage ring, ESRF, Grenoble, 1998, to be published.
[10] A. Hofmann, Characteristics of synchrotron radiation, *Proc. Cern Acc. School "Synchrotron Radiation and Free-Electron Lasers"*, Grenoble, France, 22–28 April 1996.

[11] G. Müelhaupt and C. Denise, Study of interferences with the visible synchrotron light emitted from various magnets at the ESRF. Use of optical images for diagnostic on the electron beam, (ESRF97MU193), *NIM A*, **387** (1996) 319–327; C. Denise, Etude de la lumière synchrotron émise par des quadrupôles et des champs de fuite de dipôles, PhD Thesis, ESRF and Université Paris XI, September 1996.
[12] E.G. Bessonov, On a class of electromagnetic waves, *Sov. Phys. JETP*, **53**(3) (1981).
[13] E.G. Bessonov, Conventionally strange electromagnetic waves, *NIM A*, **308** (1991) 135–139.
[14] V.G. Bagrov, M.B. Moiseev, M.M. Nikitin and N.I. Fedosov, Charged particle radiation in magnetic systems, *NIM* **195** (1982) 569–576.
[15] O. Chubar, Measurement of effective electron beam emittance using edge radiation, Kurtchatov Institute, preprint IAE-5596/14, Moscow, 1992.
[16] A.J. Burns, Measurement of intensity of synchrotron light spots for different mini-wiggler currents, CERN SL/Note 97-38 (BI), 29/04/1997.
[17] Y.-L. Mathis, P. Roy, B. Tremblay, A. Nucara, S. Lupi, P. Calvani and A. Gerschel, Magnetic field discontinuity as a new brighter source of IRSR, *Phys. Rev. Lett.*, **80**(6), (1998).
[18] R. Coisson, Angular-spectral distribution and polarization of SR from a "short" magnet, *Phys. Rev. A*, **20**(2) (1979).
[19] E.G. Bessonov, Some features of the bremsstrahlung and transition radiation, *Proc. 2nd Int. Sympos.*, "*Radiation of Relativistic Electrons in Periodic Structures*", September 1995, Tomsk, Russia.
[20] K.J. Kim, Transition undulator radiation as bright infrared source, *Phys. Rev. Lett.*, **26**(8) (1996).